In-flight characterization and compensation of the optical properties of the EIT instrument

Jean Marc Defise[a], Frédéric Clette[b], Frédéric Auchère[c]

[a] Centre Spatial de Liège, Avenue Pré-Aily, B-4031 Angleur, Belgium, jmdefise@ulg.ac.be
[b] Observatoire Royal de Belgique, Avenue Circulaire, B-1180 Bruxelles, Belgium
[c] USRA/ NASA, Goddard Space Flight Center, Greenbelt, MD

Keywords: SOHO, EUV telescope, Solar corona, instrumental response

ABSTRACT

Onboard the SOHO spacecraft, the Extreme UV Imaging Telescope (EIT) is imaging successfully the EUV solar corona since January 96. EIT is a normal incidence telescope, segmented in 4 separate quadrants. Each of those quadrants reflects extreme ultraviolet (EUV) light in a narrow bandpass defined by multilayer coatings deposited on the mirrors and by aluminum filters used to reject the visible and infrared part of the solar irradiance. The specific configuration of the optical system is generating artifacts that must be compensated in the raw solar images. However, the only information available to improve image quality comes from the continuous survey of the solar corona accomplished in flight by EIT. In-flight image characteristics and instrumental aspects are discussed in this paper, showing how methods can be derived to clean up the EIT data. The current investigations are addressing the internal vignetting, the shadow pattern of grids supporting the focal filters, the determination of the instrumental point spread function and the assessment of the telescope focussing, as well as the relation between those factors.

1 INTRODUCTION

The EIT (Extreme UV Imaging Telescope) instrument [1] is part of the SOHO scientific payload [2]. EIT is imaging the solar corona from the L1 Lagrangian point since January 96. The EIT instrument has no self-pointing capability. However, the spacecraft provides a very stable platform which keeps the instrument permanently pointed toward the Sun, with a stability better than 2 arcsec over several days. EIT is working in four narrow EUV bandpasses defined by multilayer coatings deposited on normal incidence optics: 171, 195, 284 and 304 Å [3]. At the focal plane of the telescope, a 1024 x 1024 pixel backside illuminated CCD is detecting the solar radiation. This detector is specially processed for EUV response enhancement [4]. Figure 1 gives an overview of the instrument concept and the configuration of the internal elements. The telescope section is made of an aluminum cylinder holding the mirrors ("Optical tube"). A set of 3 internal mechanisms is used to add filters in the optical beam ("Filter wheel"), to activate a mechanical shutter ("Shutter") and to select the EUV channel ("Sector mask").

The instrument went into a complete pre-flight EUV calibration program [5] [6] [7]. The mirror reflectivities, the filter transmissions and the CCD quantum efficiency were characterized. Since its first observations in January 1996, the instrument throughput showed important variations due to combined effects of radiations and ice deposit on the cooled detector [8]. Those topics will not be addressed in this paper where we only discuss the instrumental effects on the response without accounting for in-orbit aging effects.

The specific configuration of the optical system is generating artifacts on solar images. These effects are discussed and analyzed in order to set up corrective procedures. Filters, optics, thermal behavior and detector non-uniformities are considered in this paper.

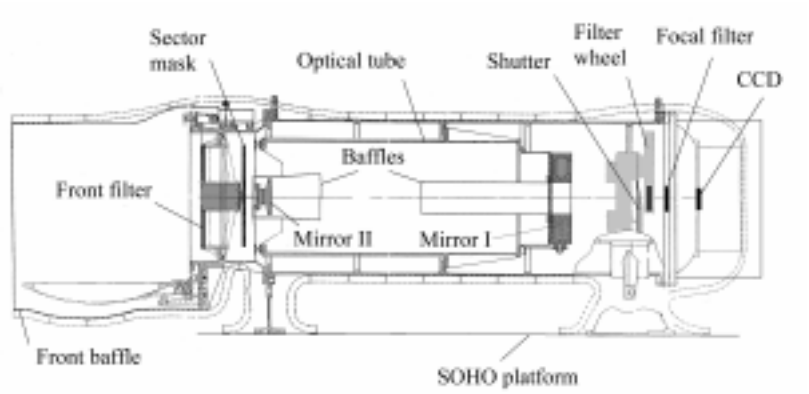

Figure 1: Schematic of the EIT instrument

2 OPTICAL SYSTEM

The telescope is a 2-mirror Ritchey Chretien design modified by Bottema and Woodruff [9], with a focal length of 1.65 m and a wide field-of-view (FOV) of 45 x 45 arcmin. In the focal plane, the CCD detector is using 1024 x 1024 square pixels of 21 µm size, that have a theoretical viewing angle of 2.6 x 2.6 arcsec.

To provide 4 EUV channels, each of the 2 mirrors is segmented in 4 separate sectors, processed with a specific stack of multilayer coating. Only one sector at a time is illuminated, as shown in figure 2 where an occulting mask is used to select the EUV channel. This 2-mirror set-up provides a 4 sub-telescope system, that produce quasi-monochromatic EUV images on the detector located in the focal plane.

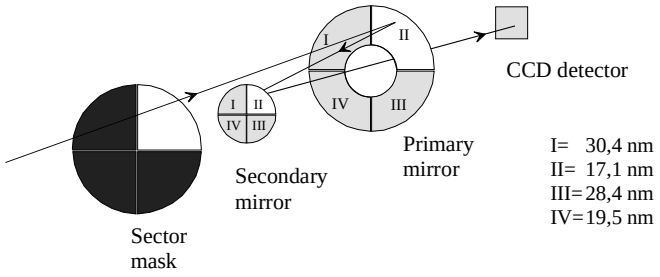

Figure 2: Optical layout of the EIT instrument

The superpolished mirrors were accurately aligned using interferometric controls [10]. The resulting wave front error is better than λ/15 peak to peak (λ=633 nm) in each separate quadrant, which will provide the 2.6 arcsec pixel resolution in the EUV. These measurements have been used to derive the EUV point spread functions (PSF) of each quadrant by using Fourier transform of the complex pupil function [11]. The resulting effective pixel FOV [12] is obtained with the convolution of the PSF and the pixel angular shape, which can also account for defocus effects. These results are shown at 304 Å in figure 3 and 4, where the angular pixel size corresponds to 2.6 x 2.6 arcsec. The optical system has been optimized for a FOV of 16 arcmin, in order to reduce the residual field curvature effects. Moreover, this FOV corresponds to the solar limb, which is a region of great interest for solar physics. With these developments, we have a tool that defines the effective FOV of each pixel, depending on the knowledge of the effective focalization.

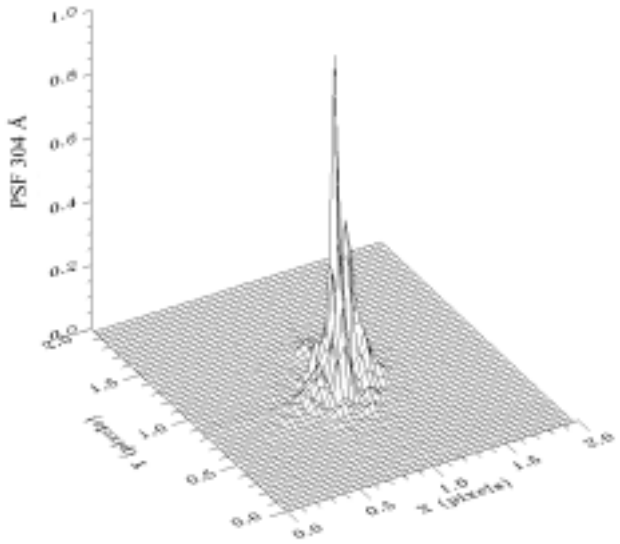

Figure 3: PSF of the 304 Å channel (for a 16 arcmin FOV)

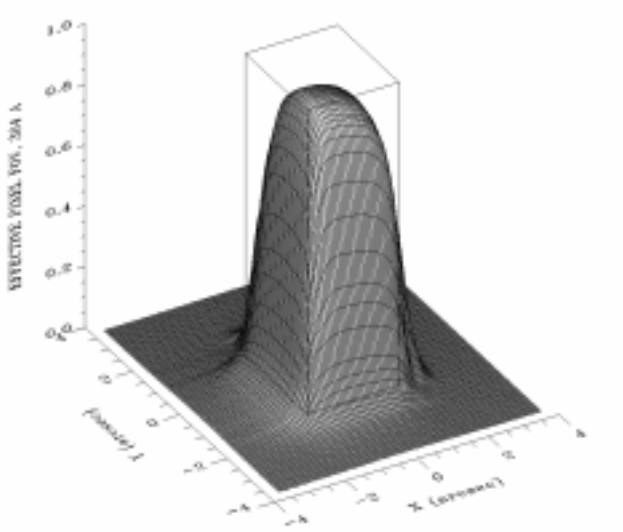

Figure 4: Effective pixel FOV obtained with the convolution of the PSF at 304 Å by the 2.6 arcsec square pixel size

3 VIGNETTING

This type of telescope usually requires the use of additional optical baffles, to avoid direct illumination of the detector without reflection on the optics. A set of 2 cylindrical baffles (fig. 1) is mounted between the mirrors to stop these unwanted rays. The drawback of this configuration is a small amount of vignetting that appears in the corners of the field of view, where it reaches locally 5.5 % (FOV=[+22.5' , +22.5'] for the 304 Å channel).

Ray-tracing studies have been conducted to construct the corresponding vignetting maps. Figure 5 shows the map of the 30.4 nm channel. The maps of the other channels can be derived from that 304 Å by 90° rotations resulting from the sub-aperture symmetry. Those maps provide a direct correction of in-flight images.
.

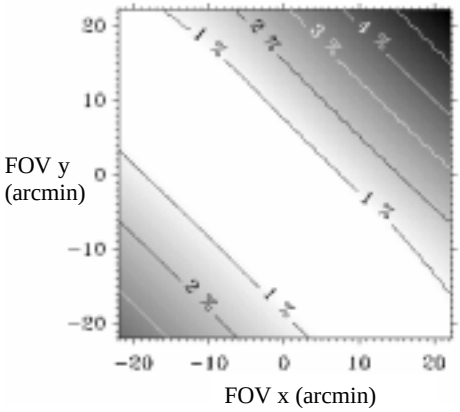

Figure 5: Vignetting map for the 304 Å quadrant. Dark regions correspond to a loss of flux intercepted by the optical baffling

4 FILTERS

4.1 Filter configuration

The EUV solar irradiation is very faint (10^{-4} W/m² for λ=304 Å) compared to the mean solar irradiance of 1370 W/m². These values define a straylight rejection goal better than 10^{8}, knowing that in the visible wavelengths the multilayered optics show a good reflectivity (40 %) and that the CCD has a high responsivity. Therefore the instrument is equipped with

filters made of thin aluminum films deposited on Ni supporting grids, which are locally opaque to EUV light. Aluminum provides a spectral window from 170 to 900 Å.

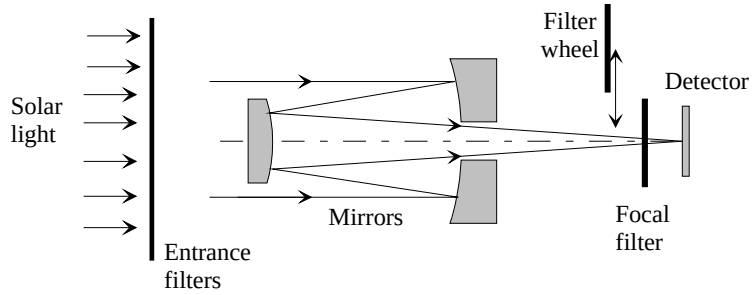

Figure 6: EUV filters in the EIT instrument.

As shown in figure 6, a set of wide filters is mounted at the entrance of the instrument in order to reject most of the IR solar radiation and to prevent internal heating. Another filter, the focal filter, is mounted close to the detector; it is used to provide the adequate overall level of straylight rejection. A filter wheel is used to insert additional filters in the EUV beam for redundancy and calibration purposes. The configuration of the EIT filters is detailed in table (1).

Table (1) : Configuration of the filters in the EIT instrument

Filter	Location	Supporting grid Mesh period	Supporting grid Rod diameter	Supporting grid Transmission
Entrance	465 mm from primary mirror	5 mm	100 µm	0,98
Focal	15 mm from focal plane	440 µm	40 µm	0,91
Wheel	30 mm from focal plane	440 µm	40 µm	0,91

4.2 Modulation of the filter grids

The opaque grids used to support the filters are interfering with the optical beam. For the entrance filters, a wide spacing mesh has been defined in order to avoid diffraction effects [10]. An additional layer of Celluloid is also used in those filters to increase the rejection of the intense He I emission line at 584 Å and to improve their mechanical properties. The focal filter is located very close to the CCD. The opaque supporting grid of this filter is responsible of shading effects that affect all the images. When filters from the wheel are inserted in the beam, additional shading effects will be combined. The modulation of the signal must be clearly identified and characterized for correction of flight data.

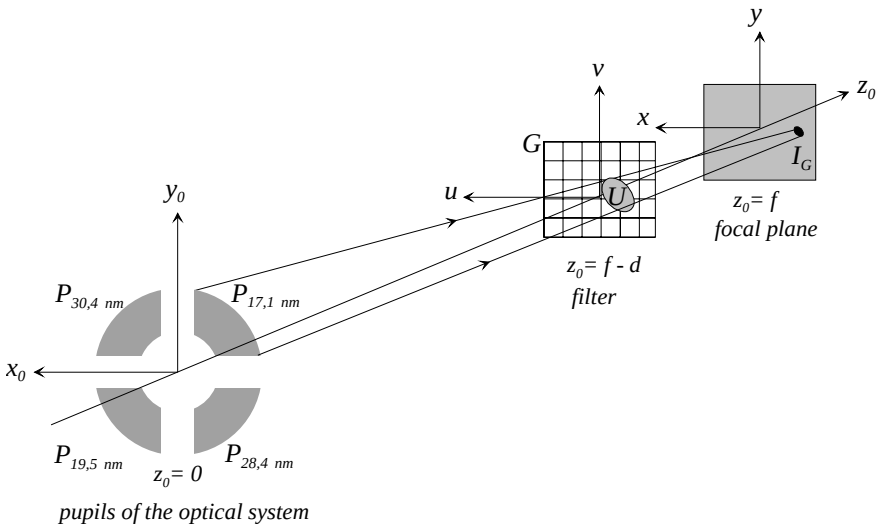

Figure 7: Shading produced by the supporting grid of the focal filter located close to the focal plane. The opaque rods intercept a fraction of the optical beam and reduce locally the focused energy.

A theoretical study has been developed to evaluate the grid effects of the permanent focal filter and to prepare efficient correction of those artifacts. With simple geometrical considerations, we can evaluate the rough shape of the modulation pattern resulting from the optical beam partly masked by the filter grid (fig. 7). If $G(u,v)$ is the grid pattern transmission (G=1 in the grid holes and G=0 in the rods) and $P(u,v)$ is the exit pupil shape (P=0 outside the pupil, P=1 inside) scaled by d/f where d is the grid-detector distance (15 mm) and f the focal length (1650 mm), then the shading function I(x,y) is given by (1). It assumes an ideal optical system.

$$I(x, y) = \iint_{u,v} P(x-u, v-y)\, G(u, v)\, du\, dv \qquad (1)$$

To improve the result, we can compute the effective shape of the optical beam after propagation in the real instrument. The exit pupil shape and the wavefront error map are introduced in the Fresnel equations [11], to derive the real wavefront in the plane of the focal grid, shown in figure 8. This accounts mostly for residual aberrations of the aligned telescope and for small diffraction effects in the EUV. An estimation of the modulation pattern resulting from the superposition of planar waves covering the field of view can be obtained by convoluting the computed intensity map with the focal grid mask and the PSF. This figure shows that the shadow of the grid produces a bright “grid” pattern, due to the relative size of the optical beam and the mesh cells. Similar results can be obtained in each quadrant that will show the same type of modulation pattern with a 90°-rotation symmetry and similar signal variations reaching a 30 % range. We obtain 4 modulation maps depending on the selected EUV channel. These results are based on several basic assumptions:

- the grids have no physical thickness (along the optical axis), otherwise grazing incidence may occur ;
- grid mesh is perfectly periodic and aligned with the pixel frame ;
- the resulting image of the beams intercepted by the grid rods is only affected by an intensity reduction and not by an additional spreading in the PSF shape ;
- the PSF measured at 16 arcmin (fig. 3) remains identical in the whole FOV ;
- the small effects of the residual field curvature are neglected.

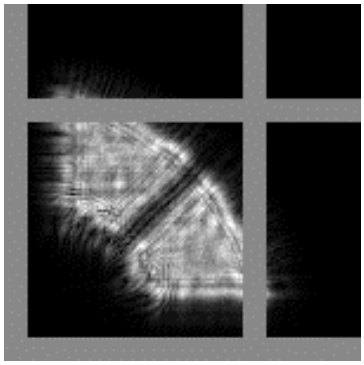

Figure 8: Computed intensity map of the wavefront at 304 Å reaching the focal filter after propagation in the instrument. The square focal grid mesh is superimposed.

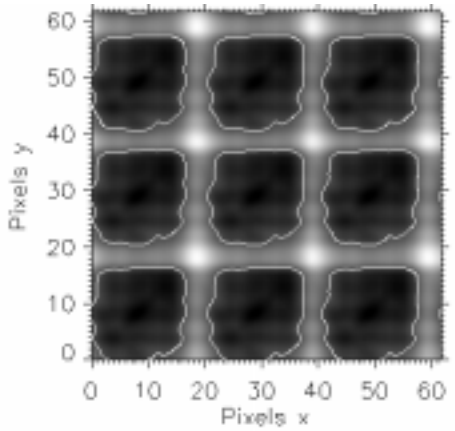

Figure 9: Theoretical modulation pattern in a 62 x 62-pixel region (using the intensity map of fig. 8 convoluted with the focal grid, the PSF and the pixel size). The unitary isocontour (white contour) is superimposed to the map to outline the shadow morphology, it indicates the neutral modulation.

This method was also used to evaluate the shading effects of the filters in the filter wheel, located at 30 mm from the detector. The resulting modulation exhibits smaller intensity variations due to the relative size of the grid and the larger optical beam.

4.3 In-flight data correction for grid modulation

The accurate positioning and orientation of the filter grid were not measured before the launch of the instrument due to late dismounting/remounting of the camera section. Therefore, with these unknowns and the related assumptions, the theoretical estimate of the modulation cannot be used to directly correct the in-flight data. A method has been developed [13] to extract a reference grid pattern in each quadrant for each filter. It is based on an average image using observations covering a solar rotation, to smooth the active solar regions and provide a better illumination of the grid pattern. After a first high-pass filtering, a 2-D median filter is applied on 5x5 pixel sets, with a 21-pixel spacing between sampled pixels in the 2 dimensions. This provides an efficient highlight of the periodic modulation. Then the power spectrum of the pattern is obtained with a Fourier transform and numerical filters are applied to isolate the harmonic peaks and derive the periodic grid pattern after inverse transform (fig. 10). The extracted patterns show the expected period and the 90°-rotation symmetry between the 4 quadrants as predicted with the grid specification and the sub-aperture configuration.

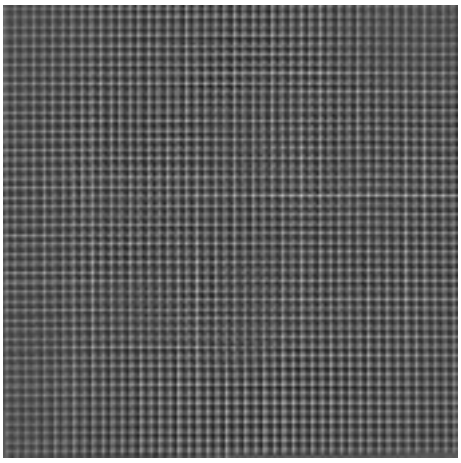

Figure 10: Extracted modulation pattern covering the whole FOV of the instrument (1024 x 1024 pixels) for the 304 Å channel.

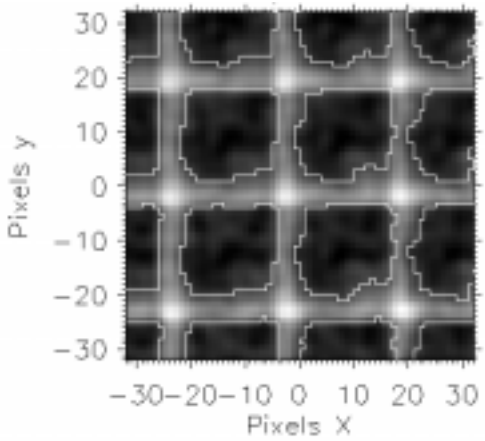

Figure 11: Enlargement of the extracted modulation pattern (central region of fig. 10, 64 x 64 pixels, 304 Å), with the superimposed unitary isocontour (white contour).

The morphology of the extracted pattern (fig. 11) shows a good similarity with the theoretical evaluation (fig. 9 for the 304 Å quadrant). The amplitude of the extracted modulations is in a good agreement with the theoretical data in all the EUV channel, as shown in table (2) where we compare the minimum and maximum values, the standard deviation.

Table (2) : Comparison of the modulations produced by the focal grid in the 4 quadrants, with the theoretical model and with the pattern extracted from the solar images.

Channel	Theoretical minimum	Theoretical maximum	Theoretical σ	Extracted minimum	Extracted maximum	Extracted σ
171 Å	0.887	1.220	6.7 %	0.904	1.196	5.1 %
195 Å	0.906	1.206	5.5 %	0.904	1.192	4.5 %
284 Å	0.896	1.208	5.8 %	0.873	1.218	4.7 %
304 Å	0.904	1.214	6.2 %	0.878	1.207	5.0 %

The same procedure is applied for the wheel filters, which showed a smaller modulation, as predicted by the theoretical model. This provides an efficient tool that can be used to correct any EIT individual image by direct matrix division. A set of reference correction maps (1024 x 1024 points) has been set up with the data recorded at the beginning of the mission. For each of the 5 combinations of filters, we built 4 reference maps to cover the 4 EUV channels. It must be outlined that the correction is less accurate when filters in the wheel are used, due to the repositioning inaccuracies that can slightly change the pattern position.

5 DETECTOR FLAT FIELDS

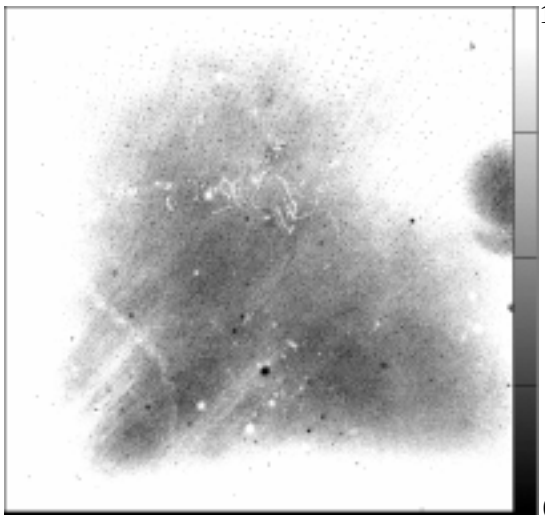

Figure 12: Pre-flight flat-field map at 195 Å. Dark regions correspond to local loss of sensitivity.

With specific thinning and ion implants, the EIT CCD detector exhibits an enhanced sensitivity for EUV observations. In each of the 4 EUV channels, it shows distinct responsivities, which were evaluated with calibration measurements. The pixel-to-pixel non-uniformities were also measured with flat-fielding. Flat-field maps at 195 and 284 Å were derived from tests with the synchrotron EUV radiation available at the IAS facility (Orsay, F) [1] [5] [6].

These maps can be used directly to correct the images of the 4 EUV channels.

However, once in orbit, the detector will experience local degradations. This will require updates of the flat-field maps due to local modification of the pixel sensitivities produced total EUV dose effects combined with contamination deposit on the cooled CCD [8].

6 FOCUS QUALITY AND THERMAL REFOCUS

The on-ground alignment was optimized at +20°C for a 16 arcmin FOV. An aluminum optical tube provides the good positioning of the mirrors. This tube is equipped with an active thermal control which is used to ensure a +20°C stable temperature (0.3 °C stability) while the instrument is subjected to variations of the thermal environment produced by the seasonal changes of the solar irradiance and by the aging of the thermo-optical properties of the coatings [14].

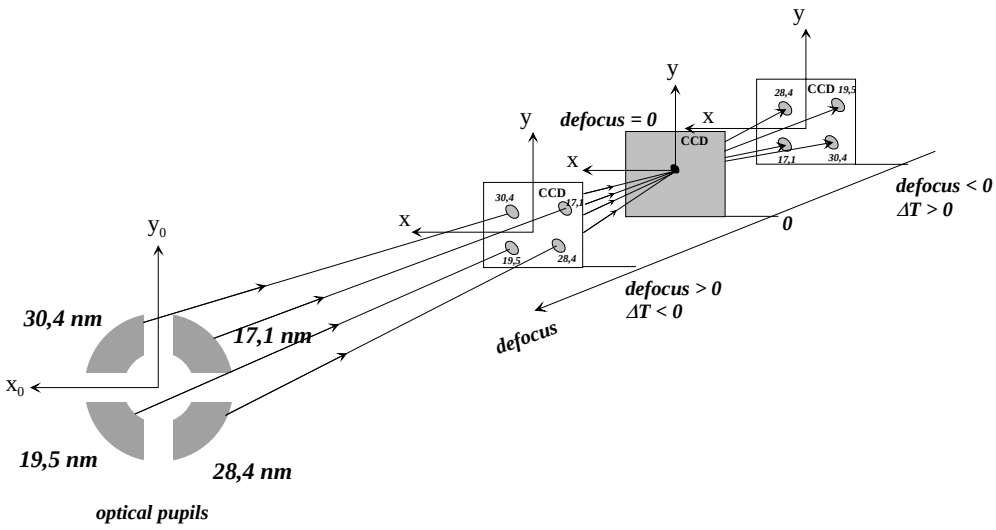

Figure 13: Schematics of the decentring associated with defocus. The decentring of the pupils appears in the focal plane when the detector is out of focus.

The in-flight thermal control can also be used to adjust the mirror spacing and modify the positioning of the focal plane to improve the focalization. The evaluation of focus quality is not straightforward, as there is no stable EUV point object in the instrument FOV. The decentring of the exit pupils of the 4 subtelescopes can be used for this purpose. If the detector matches exactly the focal plane, the images taken with each of them will be correctly centered. If the focus is not perfect, as

shown in figure 13, a decentring proportional to the defocus will appear, with a symmetry corresponding to the 4 sub-apertures. The direction of the defocus can also be correspondingly determined.

The variations of the point spread function and the corresponding effective field of view have been studied with the Fresnel propagation laws accounting for the focus variations with temperature. In figure 14, we present a result of this evaluation with the spreading and the translation of the pixel effective FOV when the optical system is heated from +20°C to +26°C. The translation is a simple geometrical effect resulting from the decenter of the pupil and the thermal defocus (fig. 13). Computed plots of the defocus (µm) and field decentring (2.6 arcsec-pixels) versus temperature are shown in figure 15.

Thanks to the very high stability of the pointing of SOHO and the constant temperature of the EIT optical system, it was possible to analyze the EIT solar images and to locate the center of the solar limb in each EUV full field image. This evaluation has the advantage of taking into account the field angle (16 arcmin) where the focussing error should be zero. The results of this analysis indicate a symmetric decentring between the 4 EUV channels, as shown in figure 16 where the daily offset of the solar limb center coordinates (x,y) is compared in each quadrant in a stable thermal configuration (T=18.3°C) during the 29 first months of the mission.

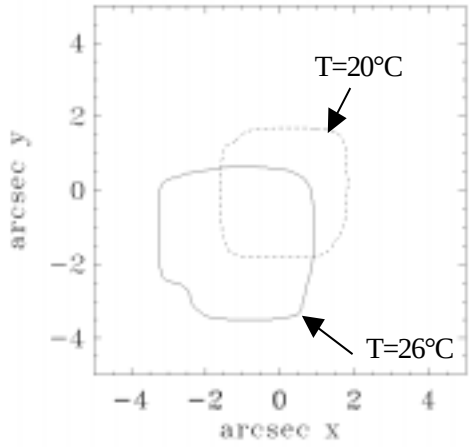

Figure 14: Spread and translation of the effective pixel FOV (304 Å) for a 6 °C heating. The plots are iso-contours of the 10 % maximum of the FOV functions (T=20°C corresponds to fig. 4).

This offset corresponds to a positive defocus of 253 µm, that could be reduced to zero with a temperature increase of 3°C. The accuracy of the method is directly dependent on the limb fitting algorithm developed to identify the center coordinates. The 304 Å channel shows the largest dispersion due to the different nature and structure of the solar limb at this wavelength.

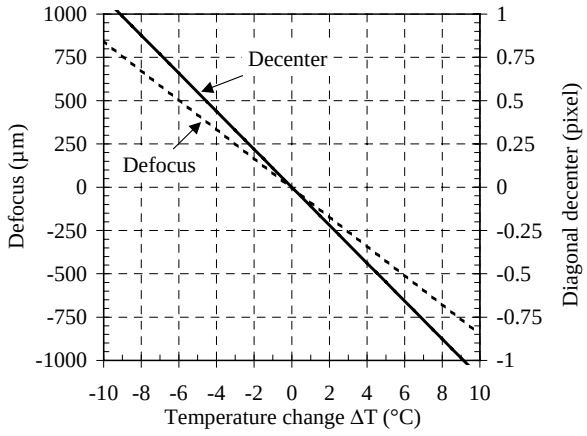

Figure 15: Theoretical estimation of the defocus and the diagonal decenter induced by thermal excursions of the telescope. The zero defocus was initially set up for a 16 arcmin FOV and a temperature of 20°C.

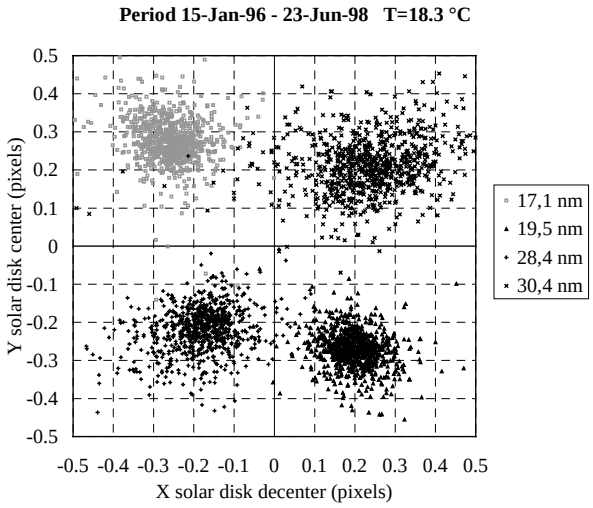

Figure 16: Decentring of the solar limb in the 4 EUV channels. This configuration corresponds to a diagonal decenter of 0,33 pixel and a positive defocus of 253 µm (axes and orientation as in fig. 13).

The optical system was heated from 18.3°C to 21°C during a few days in March 1999. The change in the solar limb decenter is reported in figure 17, which outlines the direct relationship with the temperature. This result demonstrates the ability of the thermal control to adjust the focus of the optical system on the detector. These measurements provide an efficient tool to define the effective FOV of each pixel with the characterization of the focus quality. The simple knowledge of the optics temperature gives the defocus (fig. 15), which is to be taken into account in the PSF evaluation.

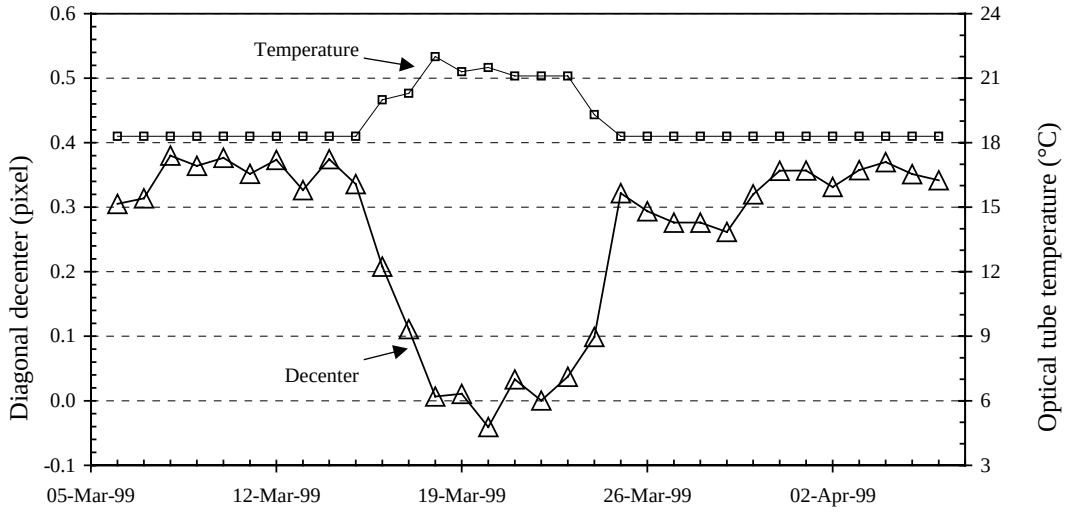

Figure 17: Averaged recentring obtained with a progressive temperature increase of 3°C from 14 to 25-Mar-99.

7 FLIGHT DATA REDUCTION

The data reduction of the EIT solar images provides all the required corrections to remove the instrumental artifacts that affect the signal. The basic procedure is shown in figure 18. The rough image is made of 1024 x 1024 14-bits digital data formatted in a FITS-standard file. The electronic offset subtraction is the first correction and is identical for all the pixels. It is only dependent on the on-board electronics and it remained constant during the 3 first years of the mission. After this first step, the resulting signal is directly proportional to the pixel irradiance. The next 3 corrections are gain adjustment and can be combined to process the signal by a single signal division.

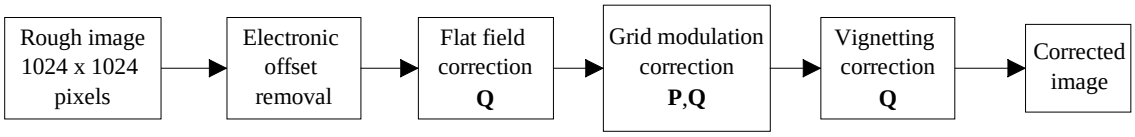

Figure 18: Basic data reduction for the EIT images before in-orbit calibration updates. These operations depend on instrumental parameters Q and P that respectively defines the EUV channel (171-195-284-304 Å) and the filter wheel selection (Clear-Al_1-Al_2-Al_3-Al_4).

This process is the first step before correcting the data for in-orbit response variations due to aging effects of the instrument.

8 CONCLUSIONS

The instrumental characteristics of the EIT telescope produce specific artifacts on the EUV solar images obtained onboard SOHO. These effects are clearly identified. With a good knowledge of the instrument, it was possible to build corrective

procedures in order to improve the scientific value of the EIT data. Those corrections are based on theoretical evaluations (vignetting), laboratory tests (flat fields), combined tests and theoretical studies (characterization of the effective FOV), in-flight measurements combined with theoretical studies (grid modulation and thermal refocus). They are implemented in a standard basic data reduction procedure to be used with the EIT level zero data. This is the first step of the general EIT data reduction that also needs to account for instrumental aging effects. The in-flight calibration showed important variations [8] which affect mainly the flat field correction. Additional developments are under study to improve and extend the EIT data processing to aging corrections, in order to produce higher-level science data.

9 REFERENCES

[1] Delaboudinière et al, "EIT: Extreme-UV imaging telescope for the SOHO mission", Solar Physics **162**: 291-312, 1995.

[2] V. Domingo, B. Fleck, A.I. Poland, "The SOHO Mission", Solar Physics **162**: 1-37, 1995.

[3] Chauvineau et al, "Description and performance of mirrors and multilayers for the Extreme ultra-violet Imaging Telescope (EIT) of the SOHO mission", SPIE **1546**, 576-586, 1991.

[4] Moses et al, "Performance of back-illuminated Tektronix CCDs in the extreme ultraviolet", SPIE **2006**, 252-257, 1993.

[5] X. Song, "Caractérisation et étalonnage radiométrique du télescope solaire EIT à l'aide du rayonnement synchrotron", Thesis, Université Paris XI, 1995.

[6] J.M. Defise, X Song, J.P. Delaboudinière, G. Artzner, C. Carabetian, J.F. Hochedez, J. Brunaud, J. Moses, R. Catura, F. Clette, A. Maucherat, "Calibration of the EIT instrument for the SOHO mission", SPIE **2517**, 29-39, 1995.

[7] K. Dere, J. Moses, J.P. Delaboudinière, J. Brunaud, C. Carabetian, J.F. Hochedez, X.Y Song, R. Catura, F. Clette, J.M. Defise, "The preflight photometric calibration of the extreme-ultraviolet imaging telescope EIT", Solar Physics, to be published.

[8] J.M. Defise, J. Moses, F. Clette and the EIT Consortium, "In-orbit performances of the EIT instrument on-board SOHO and intercalibration with the EIT Calroc Sounding rocket program", SPIE **3442**, 1998.

[9] M. Bottema, R. Woodruff, "Third order aberrations in Cassegrain-type telescopes and comma correction in servo-stabilized images", Appl Opt, **10**, 300-303, 1971.

[10] P. Rochus, "Alignment of the Extreme-UV Telescope (EIT)", Applied Optics & Optoelectronic Conference, York, 1994.

[11] J. W. Goodman, "Introduction to Fourier Optics", Mc Graw-Hill, 1968.

[12] C. L. Wyatt, "radiometric System Design", Macmillan Publishing Company, 1987.

[13] Moses et al, "EIT Observations of the Extreme Ultraviolet Sun", Solar Physics **175**: 571-599, 1997

[14] J.M. Defise, P. Rochus, "Lessons learned from the thermal design of an instrument (EIT, the Extreme-UV Imaging telescope) on board SOHO", J. Aerospace , Sec. 1 Vol. **106**, 1079-1094, 1997.

[15] J.M. Defise , J.P. Delaboudinière, R. Catura, F. Clette , J. Maucherat, "Calibration of the EIT Instrument", SPIE **2517**, 29-39, 1995.